Orbit-Spin Coupling Torques and Martian Dust Storm Activity in MY34 and MY 35

James Shirley[1], David Kass[1], and Armin Kleinböhl[1]

[1]Caltech-JPL

November 23, 2022

Abstract

One global-scale dust storm and two larger-than-average regional-scale dust storms have been recorded by spacecraft observations within the dust seasons of the past two Mars years. Each of these storms began near times when the orbit-spin coupling torques on Mars were changing most rapidly. While a clear association between Martian planet-encircling dust events and orbital torque episodes has been established (JGR-Planets 125, e2019JE006077), possible relationships between orbital/dynamical variability and regional-scale storm occurrence have not previously been investigated. In this study we compare the initiation periods and early development of the MY 34 "C" storm and the MY 35 "A" storm with prior findings obtained for the planet-encircling dust event of MY 34. We employ observations by MRO's Mars Climate Sounder to compare dust loading, atmospheric temperatures, dynamical heating indices, and dust layer peak altitudes, to illuminate the similarities and differences between these events, in juxtaposition with a discussion of the concurrent variability of the planetary orbital angular momentum and the resulting torque on Mars.

Orbit-Spin Coupling Torques and Martian Dust Storm Activity in MY34 and MY 35

James H. Shirley, David M. Kass, and Armin Kleinböhl*

Jet Propulsion Laboratory-California Institute of Technology

Pasadena, CA USA

The circulation of the Martian atmosphere is alternately spun-up and spun-down by a weak coupling between Mars' orbital and rotational motions. A reversing torque acts to add and subtract momentum to and from the large-scale circulation of the atmosphere.

1. Introduction

All of the Martian *global dust storms (GDS)* of the historic record have occurred under one or the other of the following two *forcing conditions*:

1) Global dust events tend to occur at times when orbit-spin coupling torques are peaking near the middle of the dust storm season (Fig. 1a), and

2) Global dust events also tend to occur near the times when the orbit-spin coupling torques are changing most rapidly (Fig. 1b).

**Direct correspondence to: James H. Shirley (jrocksci@att.net)*

(Torquefex, Simi Valley, California)

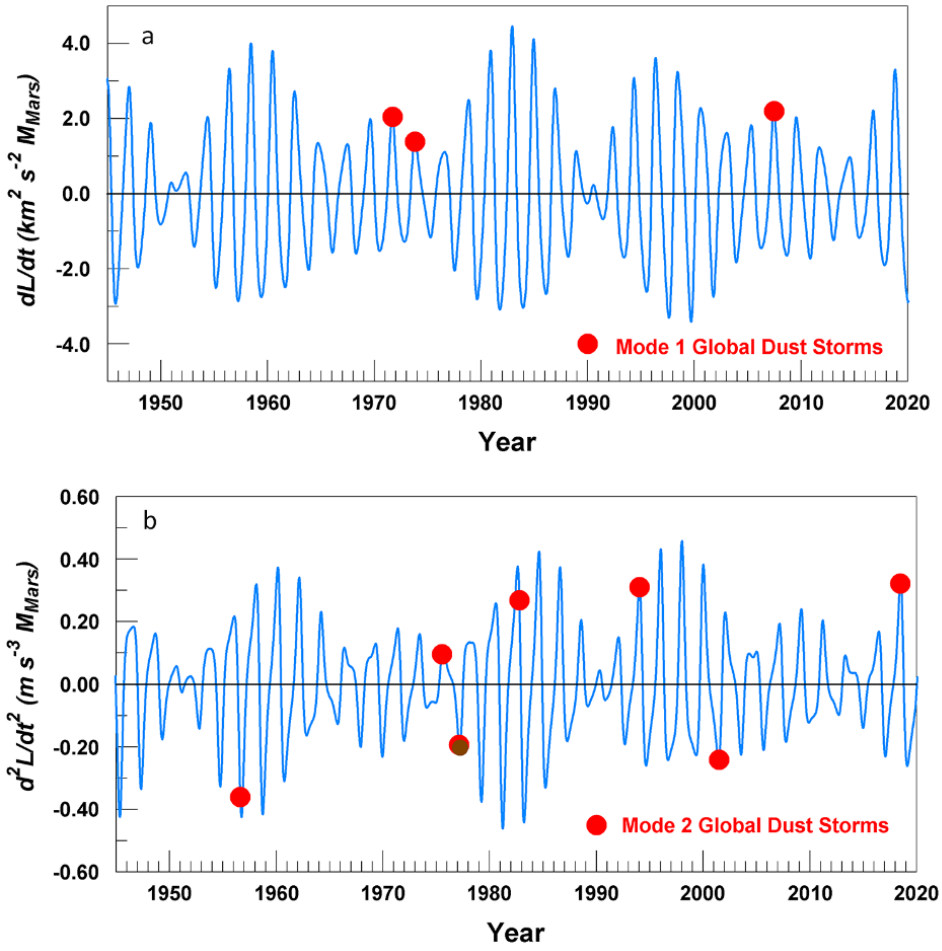

Figure 1: Occurrence times of known Martian global dust storms (1945-2020) with respect to the orbit-spin coupling forcing function dL/dt (a) and to its time derivative, d^2L/dt^2 (b). The Mode 1 category includes the GDS of 1971, 1973, and 2007. The Mode 2 category includes the recent 2018 event, along with the historic events of 1956, 1975, 1977, 1982, 1994, and 2001. After Shirley et al., 2020.

The orbit-spin coupling mechanism gives rise to *large-scale instability* of the Martian atmospheric circulation. As an aid to understanding how this occurs, we provide the following analogy. We begin with a system consisting of a hand-held kitchen mixer, together with a bowl full of cake batter. Both the speed and direction of rotation of the "beaters" may be varied by the user. Under normal conditions, mixing at moderate speeds retains the batter within the bowl. However, there are two means of introducing large-scale instability that will spill the batter (a condition we associate with the occurrence of a major dust storm on Mars). The user can maximize the torque associated with the mixing by increasing the speed to a higher level. In our analogy, this condition corresponds to the torque maxima of Figure 1a above. The second way to introduce instability within the bowl is to rapidly alter the torque, by reversing the direction of rotation of the beaters. We liken this to the situation illustrated in Figure 1b,

wherein historic global dust storms coincide in time with peaks in the rate of change of the torque.

The orbit-spin coupling hypothesis has enabled the first-ever successful years-in-advance forecast of a planetary-scale atmospheric anomaly (i.e., the Martian global dust storm of 2018) [Shirley, 2015; Shirley & Mischna, 2017]. Mars atmospheric global circulation model simulations including orbit-spin coupling [Mischna & Shirley, 2017; Newman et al., 2019] reproduce the historic record of global dust storm occurrence and non-occurrence on Mars since 1920 with a success rate approaching 80% [Shirley et al., 2019a]. Milestones in this ongoing effort are detailed in the Table at the end of this section.

Rationale for this Investigation:

While an important role for orbit-spin coupling torques in the triggering of Martian global dust events is now evident [Shirley et al. 2019b; Shirley et al., 2020; Table 1], little to no work has been performed thus far to assess possible relationships between the external torques and the occurrence of **large regional-scale dust events** (LRDE) on Mars (Figure 2).

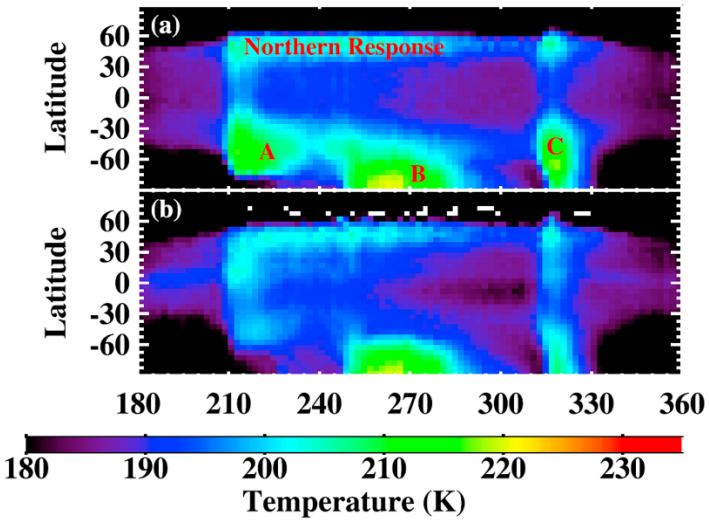

Figure 2. Zonal mean temperature structure in MY 31 at 50 Pa (~25 km) based on Mars Climate Sounder (MCS) retrieved temperature profiles. (a): Daytime temperatures; labels indicate the A, B, and C storms. (b) nighttime temperatures. Temperatures are averaged in 2° Ls intervals during the dusty season. (Kass et al., 2016).

Our goal in the present work is to initiate an investigation of this open question. To do so, we employ data describing two recent LRDE recorded by the Mars Climate Sounder Instrument (MCS) on board the Mars Reconnaissance Orbiter spacecraft. MCS data reveals that Martian years without global dust events typically exhibit three large regional events, labeled the A, B, and C storms (Kass et al., 2016). Figure 2 illustrates the timing of the A, B, and C storms in Mars year (MY) 31. Atmospheric temperatures at the 50 Pascal pressure level (found at an

altitude of about 25 km in the Mars atmosphere) reveal direct and indirect (adiabatic) atmospheric heating associated with these regional dust events.

Table 1: Timeline and milestones achieved: Orbit-spin coupling investigations

Prior Work	Principal Findings
P1: Shirley, J. H., Solar System Dynamics and Global-scale dust storms on Mars, *Icaru* s 251, 128, 2015	R1. **Discovery** of correlations linking historic Martian global dust storms (GDS) with variations in Mars orbital angular momentum with respect to inertial frames
	R2. First **published forecast** calling for a GDS in 2018
P2: Shirley, J. H., Orbit-spin Coupling and the Circulation of the Martian Atmosphere, *Planetary & Space Science* 141, 1-16, 2017	R3. **Derivation** of the **coupling equation** and demonstration of **quantitative sufficiency**
	R4. **Prediction**: Orbital variations drive cycles of intensification and relaxation of atmospheric circulations
P3: Shirley, J. H., and M. A. Mischna, Orbit-spin Coupling and the Interannual Variability of global-scale dust storm occurrence on Mars. *Planetary & Space Science* 139, 37-50, 2017	R5. First **formal statistical test** of the circulatory intensification-relaxation prediction of the orbit-spin coupling hypothesis
	R6. Second published forecast calling for a GDS in 2018
P4: Mischna, M. A., & J. H. Shirley, Numerical Modeling of Orbit-spin Coupling Accelerations in a Mars General Circulation Model: Implications for Global Dust Storm Activity, *Planetary & Space Science* 141, 45-72, 2017	R7. **Hypothesis testing** employing numerical simulations of an atmospheric circulation with orbit-spin coupling. **Confirmation** of the **prediction** of driven cycles of circulatory intensification within the modified GCM, claiming **proof of concept**
	R8. **Improved agreement with observations**: First-ever year-by-year **replication of observed planetary-scale atmospheric anomalies**, without the need to pre-condition state variables within the model
	R9. Third published forecast calling for a GDS in 2018
	R10. Identification of a **diagnostic observable**: Intermittent cycles of itensification and relaxation of **meridional overturning circulations**
P5: Newman, C. E., C. Lee, M. A. Mischna, M. I. Richardson, and J. H. Shirley, An initial assessment of the impact of postulated orbit-spin coupling on Mars dust storm variability in fully interacive dust simulation. *Icarus* 31, 649-668, 2019	R11. Second GCM investigation demonstrating **proof of concept**. The inclusion of orbit-spin coupling accelerations dramatically inproves the model's skill at predicting GDS and non-GDS years compared to a model without forcing
	R12. Fourth published forecast calling for a GDS in 2018
P6: Shirley, J. H., C. E. Newman, M. A. Mischna, & M. I. Richardson. Replication of the Historic Record of Martian Global Dust Storm Occurrence in an Atmospheric General Circulation Model, *Icarus* 317, 197-208, 2019	R13. **Improved agreement with observation**s: The MarsWRF GCM, with orbit-spin coupling, **reproduces the historic record of Martian GDS** with a success rate of **77%**.
P7: Shirley, J. H., A. Kleinböhl, D. M. Kass, L. J. Steele, N. G. Heavens, S. Suzuki, S. Piqueux, J. T. Schofield, and D. J. McCleese, Rapid Expansion and Evolution of a Regional Dust Storm in the Acidalia Corridor During the Initial Growth Phase of the Martian Global Dust Storm of 2018, *Geophysical Research Letters* 46, e2019GL084317, 2019	R14. **Real-time observation of predicted effects**: The regional -scale "triggering storm" that initiated the 2018 global dust storm was powered-up by an intensified meridional overturning circulation. Spacecraft observations unambiguously record and resolve the **diagnostic observable** for orbit-spin coupling
P8: Shirley, J. H., R. J. McKim, J. M. Battalio, & D. M. Kass, Orbit-spin Coupling and the Triggering of the Martian Planet-encircling Dust Storm of 2018, *Journal of Geophysical Research-Planet* s 125, e2019JE006077, 2020	R15. All historic Martian global dust storms are shown to be associated with dynamically and statistically defined **torque episodes**.
	R16. Sub-seasonal time resolution is achieved for hindcasting and for routine **forecasting of intervals of atmospheric instability** on Mars for the years 2020-2030

2. Orbit-Spin Coupling

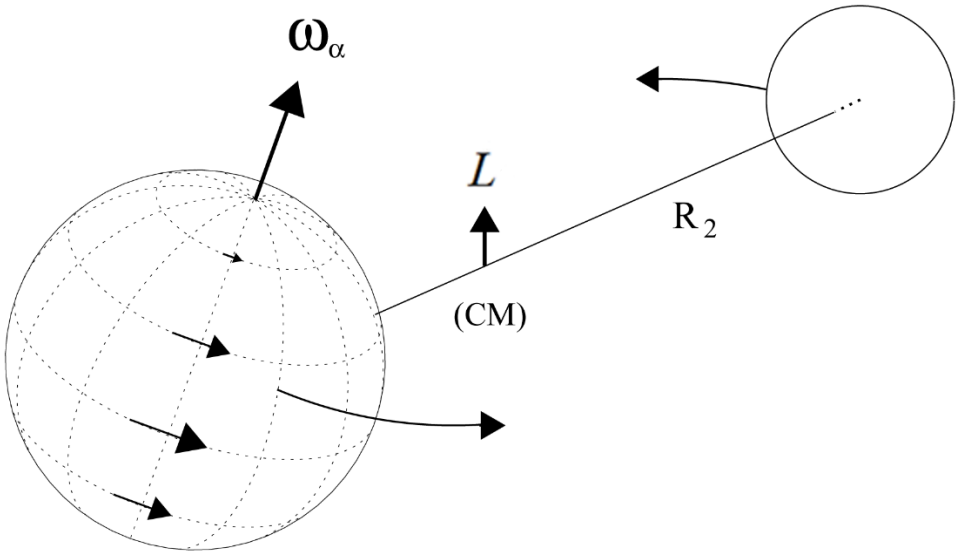

Figure 3. System diagram for spin-axis rotation and orbital revolution in a 2-body system. The curved arrows represent the orbital trajectories of a subject body (at left), and its companion, as they revolve about the center of mass (CM) or barycenter of the pair. ***L*** is a vector representation of the angular momentum of the orbital motion; its direction is normal to the orbit plane. R denotes an orbital radius extending from the body center to the system barycenter (here, labeled only for the companion body, i.e., R2). The axial rotation (or spin) of the subject body is represented by the angular velocity vector ω_α.

Figures 3 and 4 illustrate essential aspects of the orbit-spin coupling mechanism. Figure 3 shows vectors representing the axial rotation (ω_α) and the orbital revolution (***L***). These variable quantities (and/or their time derivatives) appear in the equation for the coupling term acceleration shown in Figure 4. Detailed discussions of the coupling equation are found in references 2, 3, 4, 6, and 8 of Table 1. Here we will only highlight a few key features of the coupling mechanism.

The "coupling term acceleration" is given by:

$$CTA = -c\left(\dot{L} \times \omega_\alpha\right) \times r$$

Here L (or dL/dt) is the time rate of change of the orbital angular momentum, ω_α is the angular velocity of rotation, and r is a position vector. The coupling efficiency coefficient c is to be determined through a comparison of modeling outcomes with observations

This identifies a global-scale acceleration field:

- Axial rotation carries the body "through" the field
- The accelerations are tangential to a spherical surface with radius r
- Meridional accelerations dominate in equatorial latitudes

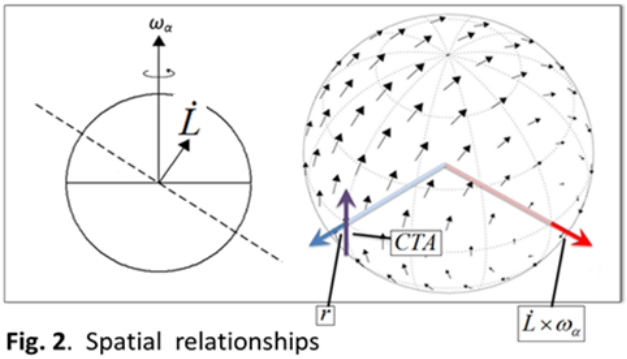

Fig. 2. Spatial relationships

Figure 4: Source of the Torque

We recognize in Figure 4 a strong similarity between the over-the-poles pattern of accelerations and the force diagram for a simple belt and pully system. The acceleration field is identified as ***a torque about an axis lying within the equatorial plane of the subject body***.

We recognize that the torque changes sign whenever the waveform of Fig. 1a crosses through zero. At such times, the acceleration field of Figure 4 diminishes, disappears, and re-emerges with oppositely-directed accelerations.

The magnitude of the accelerations is an important question. This topic is discusssed extensively in the references of Table 1. Shirley [2017] and Mischna & Shirley (2017) found (when using a *c* value of 5.0e-13) that the orbit-spin coupling accelerations were three orders of magnitude larger than the largest gravitational tidal accelerations at Mars.

In this connection, it is important to recognize that the coupling mechanism is linking and tapping extremely large reservoirs of angular momentum. Table 2 gives representative values. Here we see that the orbital angular momentum of Mars is >7 orders of magnitude larger than the rotational angular momentum of the planet. The rotational angular momentum is in turn about 8 orders of magnitude larger than the angular momentum of the Mars atmosphere [Karatekin et al, 2011]. These comparisons draw attention to the fact that **even a very tiny exchange of momentum between the orbital and rotational reservoirs may be of considerable geophysical significance**. Under the orbit-spin coupling hypothesis, the atmosphere of Mars participates in this type of exchange.

Table 2. Solar System Angular Momenta

Angular Momenta	
Solar System Total	3.15 x 10^{43} kg m^2 s^{-1}
Orbital revolution of Jupiter	1.90 x 10^{43} kg m^2 s^{-1}
Rotation of the Sun	1.92 x 10^{41} kg m^2 s^{-1}
Solar Barycentric Revolution	< 0 to >4.60 x 10^{40} kg m^2 s^{-1}
Orbital revolution of Earth + Moon	2.68 x 10^{40} kg m^2 s^{-1}
Orbital revolution of Mars	3.53 x 10^{39} kg m^2 s^{-1}
Rotation of Mars	1.91 x 10^{32} kg m^2 s^{-1}
Atmospheric circulation of Mars	~ 10^{24} kg m^2 s^{-1}

Torque Episodes

Shirley et al. [2020] make use of the correlations linking global dust storm occurrence with orbital variations of Figure 1 to identify future episodes when conditions may be favorable for the occurrence of GDS. Their specific objective was to identify, through a combination of dynamical phasing considerations and statistical analyses, future intervals that may be subject to large-scale atmospheric instability on Mars. These are termed "***torque episodes***." An example is provided in Figure 5.

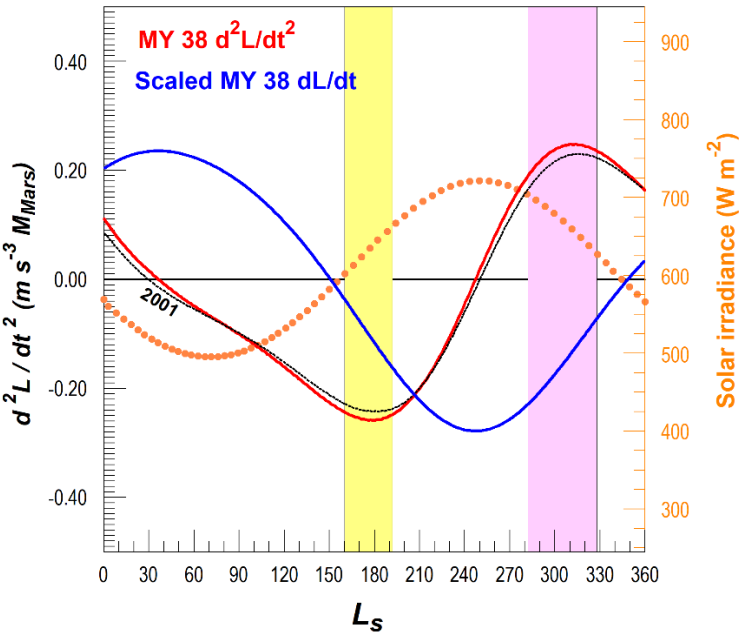

Figure 5: Forecasted torque episodes (colored bars) for MY 38 (after Shirley et al., 2020). The annual cycle of solar irradiance is indicated by orange dots. The blue curve represents the time derivative of orbital angular momentum for Mars, as in Fig. 1a. The red curve gives the second

time derivative, as in Figure 1b. A future global dust storm is considered likely to occur during the first episode (in yellow), between 24 October 2025 and 28 January 2026 [Shirley et al., 2020], due to the similarity of the d^2L/dt^2 waveform for that time period (in red) with that for the GDS year 2001 (MY 25) (black dashed line).

Shirley et al. [2020] recognized that not all of the torque episodes identified could be associated, either in the past or in the future, with global scale storms. The question of a possible association between torque episodes and LRDS, in terms of storm timing or magnitude, remains open. Thus, in this presentation, we investigate both 1) the detailed evolution of the Martian LRDS of MY 34 and MY 35, and 2) the possible relationships to the torque episodes previously identified in Shirley et al. [2020].

3. The Mars year 34 C Regional Storm

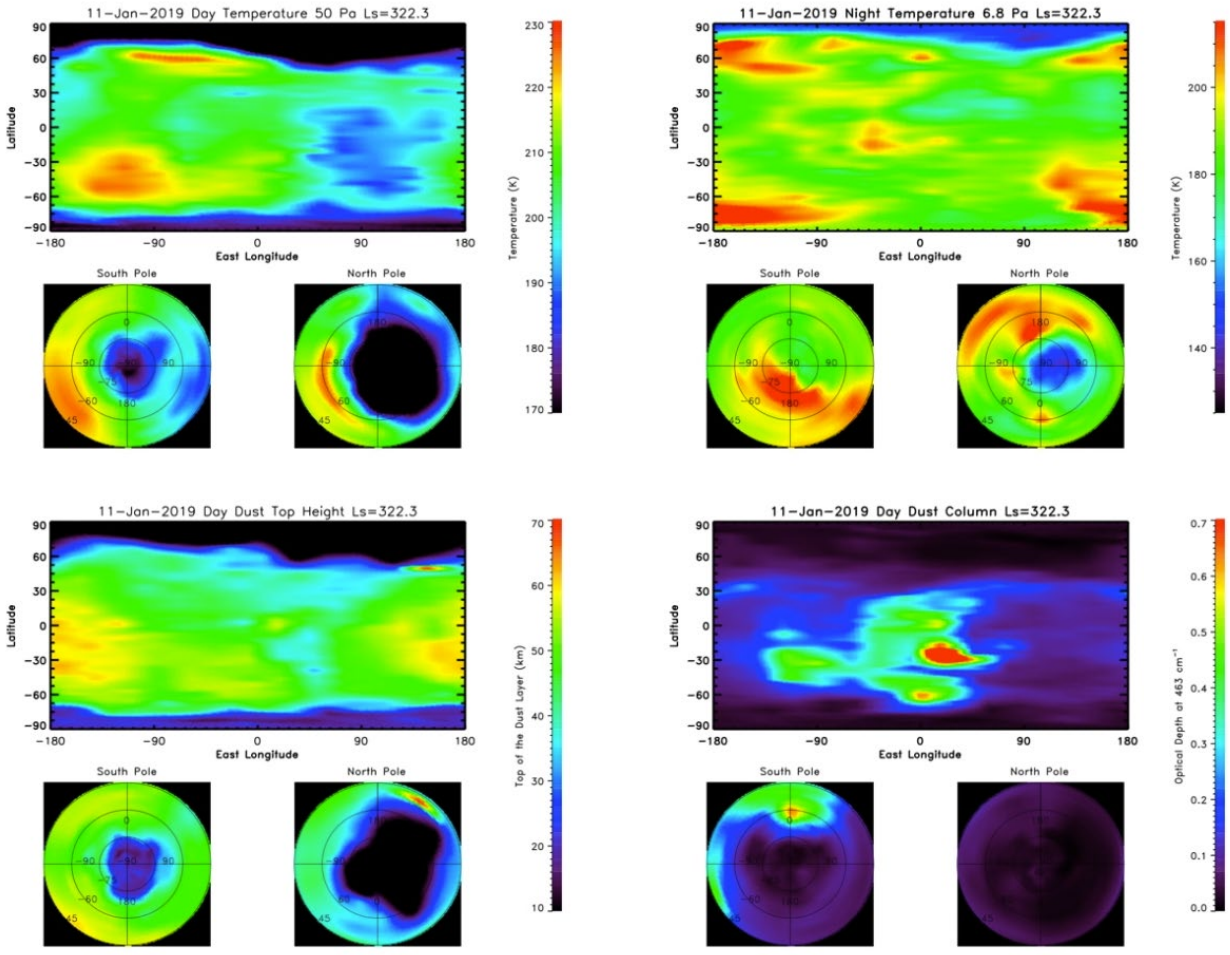

Figure 6: Movie Frame for 11 January 2019
(https://www.youtube.com/watch?v=OzKTTKgZ2G4)

Figure 6 illustrates Mars Climate Sounder (MCS) global map views of data fields investigated for large regional dust storm (LRDS) characterization. The upper views are atmospheric temperature fields and the bottom two plots represent measures of the spatial distribution of atmospheric dust. The accompanying movie illustrates the evolution of these fields from the initiation of the MY 34 C storm through its decay.

Upper left: Dayside temperatures at the 50 Pa level (~25 km altitude in the Mars atmosphere). Elevated temperatures in the western hemisphere (at left) are due to the presence of dust with associated radiative heating. Note the marked displacement of the north polar vortex (dark blue) away from its normal position (it is usually found approximately centered on the pole).

Upper right: Nighttime temperatures at the 6.8 Pa pressure level (~45 km altitude) on the same date. Nighttime heating at this altitude is not due to direct solar heating of dust, but to the adiabatic compression of the atmosphere in the downwelling branches of meridional circulation cells, which have been strengthened as a result of the dust storm.

Lower left: Altitudes (km) of the top of the dust layer. A dust extinction (km^{-1}) of 1 x 10e-4 is taken to mark the uppermost altitude of the layer. On this date an extensive area with dust layer altitudes of 55 km or higher is seen spannling the 180° meridian of longitude.

Lower right: MCS Atmospheric dust column opacity at 22 microns. The highest opacity values are found (initially) near active surface sources of dust. On subsequent days, the dust may be advected by winds to cover adjacent regions.

Features of interest appearing in the video are described in the Discussion section to follow.

Relationships to Orbit-Spin Coupling:

The early-season global dust event of 2018 took place soon after the Martian vernal equinox in MY 34. The MY 34 C LRDS occurred much later in the year, after the dust veil of the global storm had fully dissipated. The timing of both events is illustrated in Figure 7. The figure shows that both storms occurred at times when the d^2L/dt^2 waveform (also shown in Figure 1b) was approaching extreme (peak) values. At the illustrated times, the orbit-spin coupling torques were in each case changing rapidly.

The negative extreme value of the d^2L/dt^2 waveform occurred at Ls = 340. By the criteria developed in Shirley et al. [2020], this is too late in the year to qualify as an episode that could host a global dust event. However, as indicated earlier, some degree of large-scale atmospheric instability is nonetheless an expected outcome at such times.

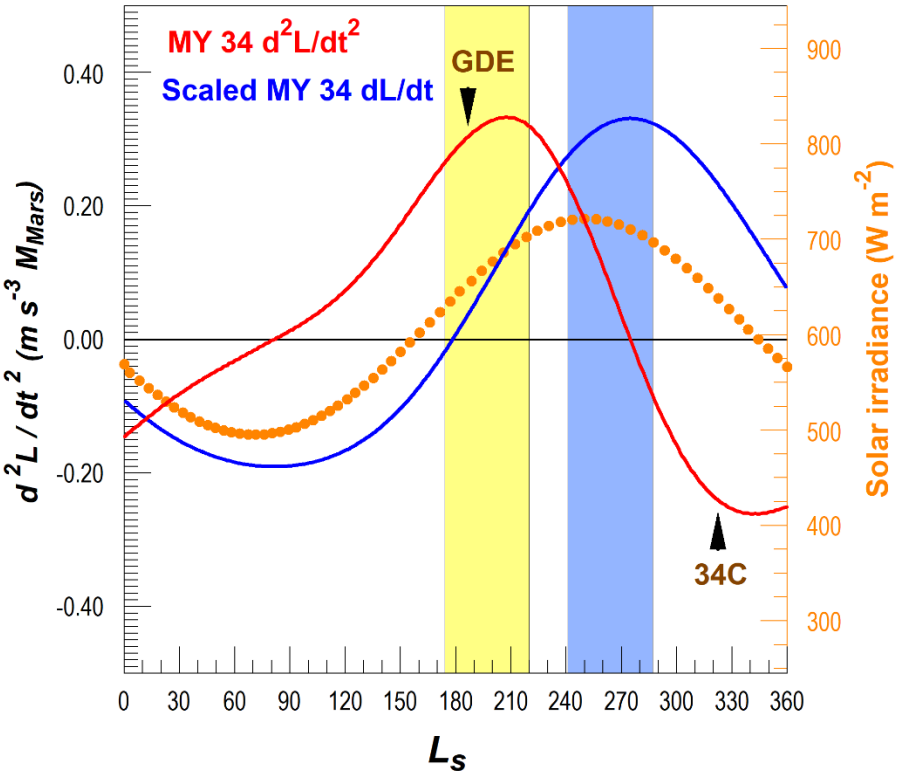

Figure 7. Dynamical waveforms, dust storm inception dates (arrowheads), and torque episodes (colored bars) for Mars year 34 [after Shirley et al., 2020]. The orange dotted line indicates the annual cycle of solar irradiance at Mars.

4. The Mars year 35 A Regional Storm

Figure 8 illustrates Mars Climate Sounder (MCS) global map views of data fields investigated for large regional dust storm (LRDS) characterization. The upper views are atmospheric temperature fields and the bottom two plots represent measures of the spatial distribution of atmospheric dust. The accompanying movie illustrates the evolution of these fields from the initiation of the MY 35 A storm through its decay.

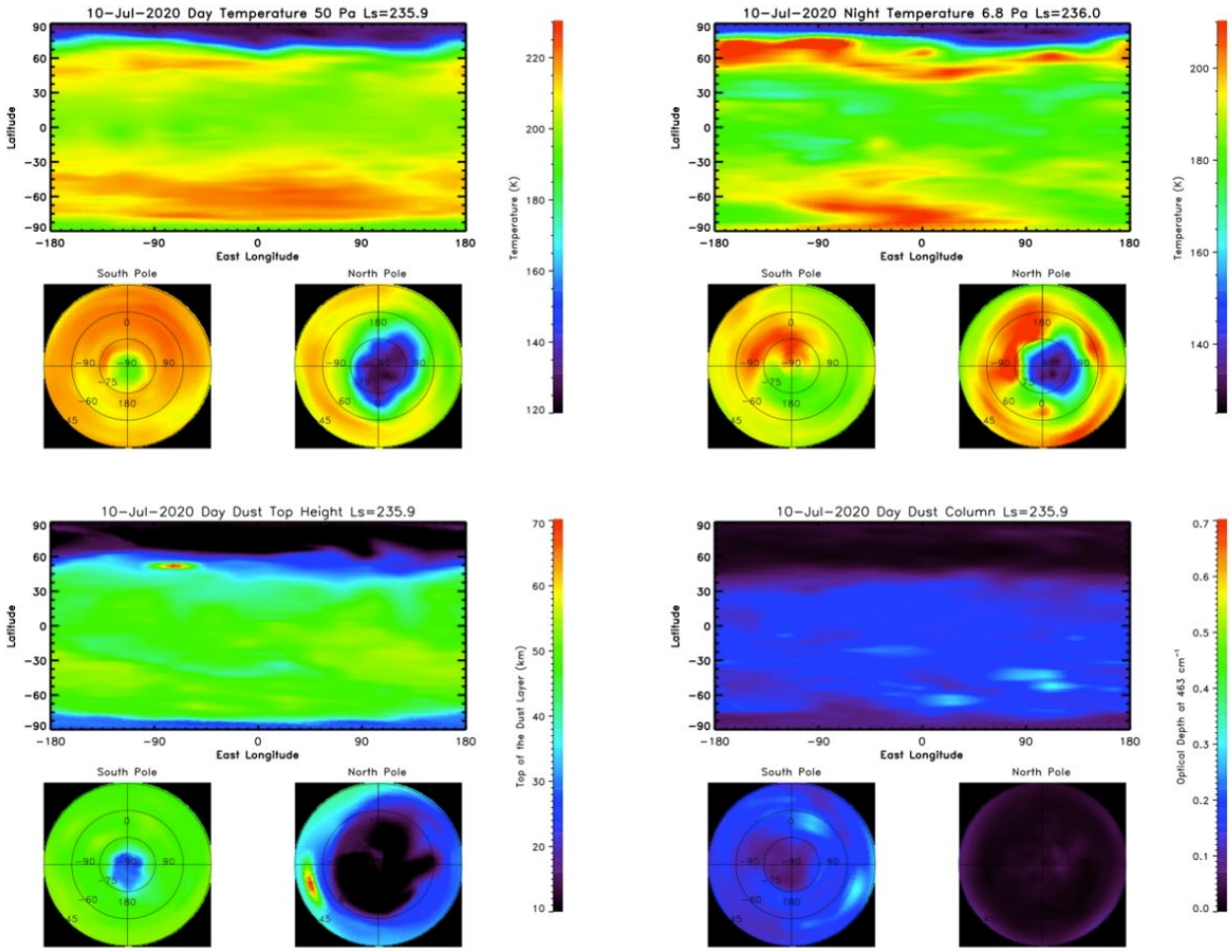

Figure 8: Movie frame for 10 July 2020. (https://www.youtube.com/watch?v=l_dH3nGJV5A)

Upper left: Dayside temperatures at the 50 Pa level (~25 km altitude in the Mars atmosphere). Elevated temperatures in the southern hemisphere are due to the presence of dust with direct solar heating. Here also we note the marked displacement of the north polar vortex (dark blue) away from its normal position (approximately centered on the pole).

Upper right: Nighttime temperatures at the 6.8 Pa pressure level (~45 km altitude) on the same date. Nighttime heating at this altitude is not due to direct solar heating of dust, but to the adiabatic compression of the atmosphere in the downwelling branches of meridional circulation cells in both northern and southern hemispheres.

Lower left: Altitudes (km) of the top of the dust layer. A dust extinction (km-1) of 1 x 10e-4 is taken to mark the uppermost altitude of the layer. On this date little variability of dust layer height with longitude is seen.

Lower right: MCS Atmospheric dust column opacity at 22 microns. Few areas with appreciable dust column opacity are seen for this date.

Features of interest in the MY 35A video are described in the Discussion section that follows.

Relationships to Orbit-Spin Coupling

An equinoctial torque episode was identified for MY 35 in Shirley et al. [2020], as illustrated by the yellow bar in Fig. 9. However, the authors did not issue a favorable forecast for a global dust storm in MY 35, due to concerns about the phasing of the dynamical waveforms with respect to the annual cycle, together with ambiguous indications from the historic record.

As indicated in Figure 9, the MY 35 A storm began close to the time when the orbit-spin coupling torque was changing most rapidly.

While this presentation was in preparation, an additional MY 35 LRDS was detected. The timing of this storm is also indicated in Figure 9. The storm began just after a peak in the dL/dt waveform. This is similar to the relationships illustrated for historic global dust storms in Figure 1a, including the 2007 GDS.

The methodology of Shirley et al. [2020] did not identify a torque episode (a candidate interval for global-scale storm occurrence) at this time, due to the delayed occurrence of the peak of the dL/dt waveform with respect to the annual cycle. Nonetheless, under the orbit-spin coupling hypothesis, times when the torque is peaking are recognized as times when the atmosphere may exhibit large-scale instability, which is in turn considered to a factor favorable for dust storm occurrence.

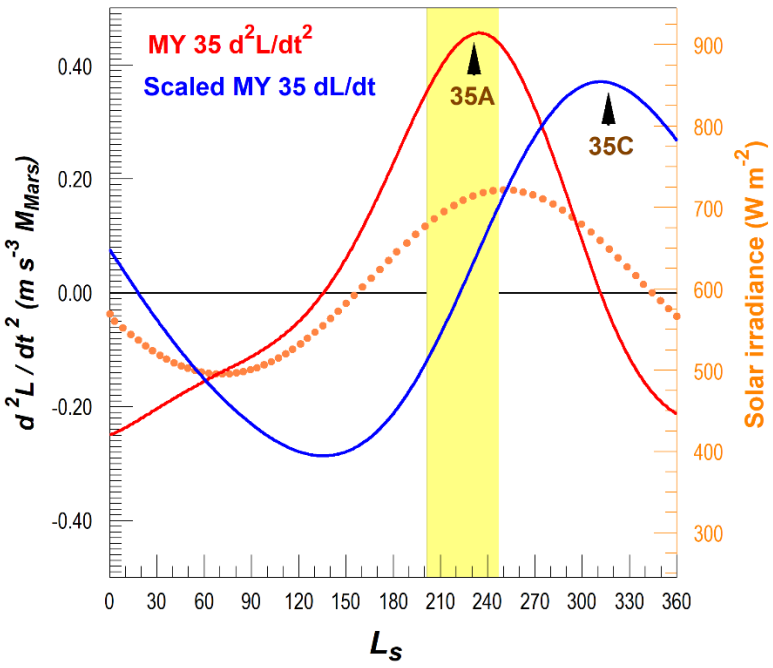

Figure 9. Dynamical waveforms, torque episodes (colored bars), and LRDS inception dates (arrowhead symbols) for MY 35. Color coding is as described for Figures 5 and 7.

5. Results and Discussion

Comparing and Contrasting LRDS (and GDS)

A wealth of information is captured in the video clips for the MY 34 C and MY 35 A LRDS. We here list a few of the key similarities and differences amongst and between these storms. For comparison purposes we may also draw on the study by Shirley et al. [2019b] of the 2018 regional "triggering storm" that preceded the global dust event of that year.

In what ways are the studied LRDS similar to the GDS of 2018? We note two factors of interest. First, within both video clips, we observe that high values of the dust column opacity, in the earliest days of both LRDS, were initially localized between the longitudes of 0 and 90 W. The same was true for the 2018 Acidalia Corridor triggering storm [Shirley et al., 2019b].

The LRDS also bear a strong similarity to the GDS of 2018 in exhibiting marked displacements of the northern polar vortices that persisted for considerable periods of time during the storms. Kleinböhl et al. [2020] document this displacement in the case of the GDS. Here we note that marked asymmetries and displacements of the vortices (away from their typical positions, centered over the pole) persisted for more than 2 weeks (from January 6 to January 21) in the 34 C LRDS. In the case of the MY 35 A LRDS, significant displacements of the northern polar vortex were observed between 26 June and 19 July (2020).

In what ways do the studied LRDS differ from the 2018 GDS? A number of investigators have examined this question; we will not pause here to review the many prior findings. Working from the data at hand, we recognize two significant differences. One is found in the number of dust-lifting centers activated. In both video clips, we observe in the column opacity plots that the principal dust lifting activity was within and adjacent to the Acidalia storm track. In the 35A case, there is some ambiguity regarding dust lifting locations in the mature phase of the storm. Future work incorporating MARCI imaging data should resolve this ambiguity. In any case, it is clear that many more lifting centers were activated in the 2018 GDS [Shirley et al. 2019b; Heavens et al. 2019] than in either of the LRDS investigated here.

A second difference between the LRDS evaluated here and the 2018 triggering regional event (and the subsequent GDS) [Shirley et al., 2019b] is found in the peak altitudes of dust layers in the atmosphere. In the 2018 triggering storm, dust was rapidly lofted to altitudes >70 km in the first few days of the dust event, thereafter rising even higher during the mature phase of the GDS. In the video clips for the LRDS investigated here, dust lofting to 60 km was only observed on 2 days during the 34 C storm (on January 13-14). No dust lifting to this altitude was observed throughout the 35 A storm.

In what ways were the 34 C and 35 A storms similar? We have already noted that initial dust lifting in both cases may have been concentrated in or near the Acidalia storm track. We note in addition that the impacts of both storms were most strongly seen in the western hemisphere in the earliest days (see Fig. 6 and January 8-13 in the 34 C video clip, and July 1-3 in the 35 A video clip).

Finally, we note that the 34 C and 35 A LRDS were dissimilar in a number of ways. One first order difference is found in the times required for full development to a mature phase. The MY 34 C event developed rapidly, with the first signs of the storm appearing on 6 January, peaking thereafter between 11 and 16 January (depending on the metric used). The 35 A event developed more slowly, with intermittent activity in the column opacity plots beginning about 21 June. The peak phase of the storm began sometime in the second week of July.

Relationships to orbit-spin coupling

Our sample size of LRDS events is too small to allow us to draw firm conclusions regarding the relationship or lack of relationship between orbit-spin coupling torques and LRDS. All that may be said at this point is that all four of the large storms shown in Figures 7 and 9 began near times when 1) the orbit-spin coupling torques were peaking, or 2) near times when the orbit-spin coupling torques were changing most rapidly. These coincidences dovetail with the patterns noted for historic GDS events as illustrated in Figure 1. A more comprehensive evaluation, employing a larger catalog of LRDS events, is clearly needed.

This preliminary investigation did not consider the "B storms" category of LRDS, which typically occur near the middle of the dust storm season [Kass et al., 2016]. In MY 34, the atmospheric effects of the global storm extended into the period when B class LRDS normally occur. In MY 35, an unremarkable B storm occurred. With reference to Figure 7, we show no dynamical condition that could be expected to produce an intensification of the circulation at that time.

It is of interest to additionally consider the upcoming Martian dust storm season of MY 36. As indicated in Figure 10, while the dynamical waveforms show a number of extrema, none of these has phasing (with respect to the annual cycle) that is favorable for global-scale storm occurrence. As in Shirley et al. [2020], the gray bar indicates a "transitional" year peak. Prior years with similar phasing (including the 1998 and 2013 seasons, as shown) have not produced any global-scale dust storms.

Thus, while increased large-scale atmospheric instability may occur near the vernal equinox (Ls ~ 180) and near perihelion (Ls ~ 250), no global-scale storms are considered likely to occur in MY 36. The inception dates, durations, and magnitudes of the A, B, and C LRDS in MY 36 will provide additional data to further illuminate and constrain the possible relationships between LRDS and the torques due to orbit-spin coupling.

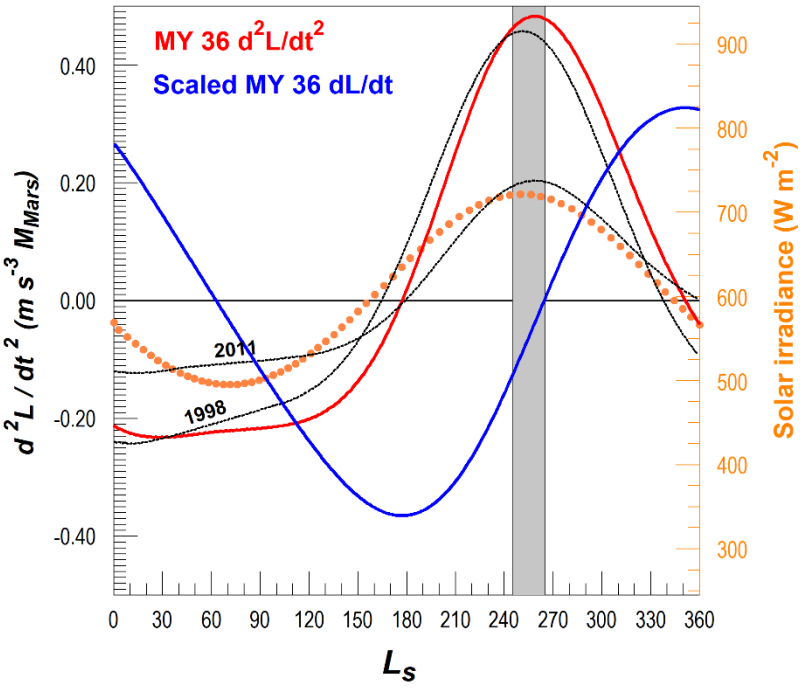

Figure 10. Dynamical waveforms and identified torque episodes (gray bar) for MY 36. Waveforms for prior years (1998, 2013) with similar phasing are shown for comparison. MY 36 is a "transitional year" [Shirley & Mischna, 2017], which is (historically) unfavorable for global-scale dust storm occurrence.

References and Acknowledgements

Acknowledgements and Data

Mars Climate Sounder data covering the period of the 2018 global dust event is available on the Planetary Data System. We acknowledge with thanks many discussions with members of JPL's Mars Climate Sounder Science and Operations Teams, including Dan McCleese, David Kass, Armin Kleinböhl, Tim Schofield, Rich Zurek, Shigeru Suzuki, Tina Tillmans, and Jason Matthews.

Algorithms for calculating solar system barycentric orbital angular momentum and its derivatives are described in references 1, 3, and 4 of Table 1. Basic data for dynamical calculations was obtained from JPL's Horizons system (https://ssd.jpl.nasa.gov/horizons.cgi).

We acknowledge support from JPL's Research and Technology Development Program and NASA's Solar System Workings Program during the early stages of this project. Portions of this work were performed at the Jet Propulsion Laboratory, California Institute of Technology, under a contract from NASA.

References

Heavens, N. G., Kass, D. M., & Shirley, J. H. (2019). Dusty deep convection in the Mars year 34 planet-encircling dust event. Journal of Geophysical Research-Planets, 124(11), 2863–2892. https://doi.org/10.1029/2019JE006110

Karatekin, Ö., de Viron, O., Lambert, S., Dehant, V., Rosenblatt, P., Van Hoolst, T., and Le Maistre, S., 2011. Atmospheric angular momentum variations of Earth, Mars, and Venus at seasonal time scales. Planetary and Space Science 59, 923–933. http://dx.doi.org/10.1016/j.pss.2010.09.010

Kass, D. M., Kleinböhl, A., McCleese, D. J., Schofield, J. T, & Smith, M. D. (2016). Interannual similarity in the Martian atmosphere during the dust storm season, Geophysical Research Letters 43, 6111-6118. 10.1002/2016GL068978

Kleinböhl, A., Spiga, A., Kass, D. M, Shirley, J. H., Millour, E., Montabone, L., & Forget, F. (2020). Diurnal variations of dust during the 2018 global dust storm observed by the Mars Climate Sounder. Journal of Geophysical Research-Planets, 125(1). https:doi.org/10.1029/2019JE006115

Mischna, M. A., & Shirley, J. H. (2017). Numerical Modeling of Orbit-Spin Coupling Accelerations in a Mars General Circulation Model: Implications for Global Dust Storm Activity, Planetary and Space Science 141, 45–72. (P4) doi: 10.1016/j.pss.2017.04.003

Newman, C. E., Lee, C., Mischna, M. A., Richardson, M. I., & Shirley, J. H. (2019). An initial assessment of the impact of postulated orbit-spin coupling on Mars dust storm variability in fully interactive dust simulations, Icarus 317, 649-668. https://doi.org/10.1016/j.icarus.2018.07.023

Shirley, J. H. (2015). Solar system dynamics and global-scale dust storms on Mars, Icarus, 252, 128–144. doi: 10.1016/j.icarus.2014.09.038

Shirley, J.H. (2017). Orbit-spin coupling and the circulation of the Martian atmosphere, Planetary and Space Science 141, 1–16. doi: 10.1016/j.pss.2017.04.006

Shirley, J. H. & Mischna, M.A. (2017). Orbit-spin coupling and the interannual variability of global-scale dust storm occurrence on Mars, Planetary and Space Science 139, 37–50. doi: 10.1016/j.pss.2017.01.001

Shirley, J. H., Newman, C. E., Mischna, M. A., & Richardson, M. I. (2019a). Replication of the historic record of Martian global dust storm occurrence in an atmospheric general circulation model, Icarus 317, 192-208. https://doi.org/10.1016/j.icarus.2018.07.024

Shirley, J. H., Kleinböhl, A., Kass, D. M., Steele, L. J., Heavens, N. G., Suzuki, S., Piqueux, S., Schofield, J. T., & McCleese, D. J. (2019b). Rapid expansion and evolution of a regional dust storm in the Acidalia Corridor during the initial growth phase of the Martian Global dust storm of 2018, Geophysical Research Letters 46. https://doi.org/10.1029/2019GL084317

Shirley, J. H., McKim, R. J., Battalio, J. M., & Kass, D. M. (2020). Orbit-spin coupling and the triggering of the Martian planet-encircling dust storm of 2018. Journal of Geophysical Research: Planets, 125, e2019JE006077. https://doi.org/10.1029/2019JE006077